


First-principles investigation of mechanical and thermal properties of MAIB ($M = \text{Mo}, \text{W}$), Cr_2AlB_2 , and Ti_2InB_2

Salawu Omotayo Akande¹,¹ Bipasa Samanta,¹ Cem Sevik^{2,3},^{2,3} and Deniz Çakır^{1,*}

¹*Department of Physics and Astrophysics, University of North Dakota, Grand Forks, North Dakota 58202, USA*

²*Department of Physics & NANOlaboratory Center of Excellence, University of Antwerp, Groenenborgerlaan 171, Antwerp B-2020, Belgium*

³*Department of Mechanical Engineering, Faculty of Engineering, Eskisehir Technical University, Eskisehir 26555, Turkey*

 (Received 29 March 2023; revised 17 July 2023; accepted 5 October 2023; published 25 October 2023)

The atomically laminated layered ternary transition-metal borides (the MAB phases) have demonstrated outstanding properties and have been applied in various fields. Understanding their thermal and mechanical properties is critical to determining their applicability in various fields such as high-temperature applications. To achieve this, we conducted first-principles calculations based on density-functional theory and the quasiharmonic approximation to determine the thermal expansion coefficients, Grüneisen parameters, bulk moduli, hardness, thermal conductivity, electron-phonon coupling parameters, and the structural and vibrational properties of MoAlB, WAlB, Cr_2AlB_2 , and Ti_2InB_2 . We found varying degrees of anisotropy in the thermal expansion and mechanical properties in spite of similarities in their crystal structures. MoAlB has a mild degree of anisotropy in its thermal expansion coefficient (TEC), while Cr_2AlB_2 and WAlB display the highest level of TEC anisotropy. We assessed various empirical models to calculate hardness and thermal conductivity, and correlated the calculated values with the material properties such as elastic moduli, Grüneisen parameter, Debye temperature, and type of bonding. Owing to their higher Grüneisen parameters, implying a greater degree of anharmonicity in lattice vibrations and lower phonon group velocities, MoAlB and WAlB have significantly lower lattice thermal conductivity values than those of Cr_2AlB_2 and Ti_2InB_2 . The hardness and lattice thermal conductivity of MAB phases can be predicted with high accuracy if one utilizes an appropriate model.

DOI: [10.1103/PhysRevApplied.20.044064](https://doi.org/10.1103/PhysRevApplied.20.044064)

I. INTRODUCTION

The atomically laminated layered ternary transition-metal borides (so called MAB phases, where M represents a transition metal) are a class of materials that have recently attracted great scientific attention due to their unique properties [1–3]. These materials are composed of alternating layers of transition-metal borides and group-A elements, which form a crystal structure known as a “lamellar” structure. The MAB phases exhibit a range of interesting properties, including relatively high hardness values, high melting points, good electrical conductivities, and high oxidation and thermal shock behavior resistance, with potential applications in areas such as wear-resistant coatings, catalysis, energy storage, and electronics. The thermal stability and oxidation resistance of MAB phases make them ideal candidates for use in high-temperature applications, such as turbine blades and other components in jet engines. Some examples of MAB phases include

$M_2\text{AlB}_2$ (space group $Cmcm$) [4,5], MAIB (space group $Cmcm$) [6], and $(\text{CrB}_2)_n\text{CrAl}$ ($n = 1-3$) [1]. The recent discovery of hexagonal symmetry in Ti_2InB_2 has provided an opportunity for exploring the possibility of expanding the composition and structure space of the MAB phases [7].

Understanding the thermal and mechanical properties of a material is essential for its applications, as these properties determine how the material behaves under different conditions, and whether or not it is suitable for specific applications. Thermal properties, such as thermal conductivity, specific heat capacity, and thermal expansion coefficient, determine how the material will conduct heat and respond to temperature changes. Similarly, mechanical properties, such as hardness, elastic constants, and ductility, determine the resistance of the material to deformation, fracture, and wear. These properties are very critical for applications including coating, cutting tools, high-temperature applications, and biomedical implants.

To enhance the applications of MAB phases in extreme environments (such as at high temperatures where the

*deniz.cakir@und.edu

temperature change is abrupt), a detailed investigation of their mechanical and thermodynamic properties is essential. Importantly, the crystal symmetry and anisotropic behavior can have a significant impact on the thermal and mechanical properties of materials. For example, materials with lower crystal symmetry tend to be more anisotropic, meaning that their properties vary depending on the direction of measurement. The anisotropic nature of materials gives rise to several distinct characteristics. Firstly, different thermal expansion coefficients can exist in different directions, leading to stress and strain within the material and ultimately impacting its mechanical properties [8–11]. Secondly, variations in strengths and stiffnesses across different directions can render materials more vulnerable to failure along specific orientations [9,12]. Lastly, materials can exhibit different electrical and thermal conductivities in different directions, influencing the flow of heat and electricity through them [13]. Collectively, these anisotropic properties underscore the importance of considering directional dependencies when studying and designing materials for specific applications.

In this respect, we employed density-functional theory (DFT) calculations combined with the quasiharmonic approximation (QHA) to elucidate the mechanical and thermal properties of MoAlB, WAIB, Cr₂AlB₂, and Ti₂InB₂. Our work includes the determination of various mechanical and dynamical properties, such as lattice vibrations at different volumes (to apply the quasiharmonic approximation and calculate Grüneisen parameters), elastic constants, bulk and shear moduli, Poisson's ratio, and several other mechanical quantities to identify the degree of anisotropy in mechanical properties. Also, we calculated thermal expansion coefficients and lattice parameters as a function temperature. By applying various empirical models combining mechanical and thermal parameters, we assessed the validity of these models in the calculation of hardness and thermal conductivity. We compared our results with available experimental results to validate our work and methodology.

II. COMPUTATIONAL DETAILS

The density-functional-theory plane-wave code VASP (Vienna *ab initio* simulation package) [14–17] and the Perdew-Burke-Ernzerhof (PBE) flavor [18] of the generalized gradient approximation (GGA) [19] were employed. We relaxed the lattice parameters and atomic positions fully while employing a Monkhorst-Pack scheme for the integration of the Brillouin zone. The k mesh is chosen according to the size of the simulation cell. The kinetic-energy cutoff of the plane-wave basis of 520 eV was found to be sufficient. The total energy convergence and maximum force values were set to 10^{-8} eV and 10^{-4} eV/Å. We employed different k meshes to calculate various properties in our study. Specifically, for structural relaxations,

we used a $16 \times 4 \times 16$ k mesh for MoAlB and Cr₂AlB₂, and a $16 \times 16 \times 8$ k mesh for Ti₂InB₂. To ensure accurate phonon calculations, the k meshes were adjusted in proportion to the dimensions of the supercells. For instance, we utilized a $4 \times 4 \times 4$ k mesh for a $4 \times 1 \times 4$ MoAlB supercell. In order to determine the elastic constants, a gamma-centered $24 \times 6 \times 24$ k mesh was employed for MoAlB and Cr₂AlB₂, while Ti₂InB₂ utilized a gamma-centered $20 \times 20 \times 10$ k mesh. These choices of k meshes ensure accurate and reliable calculations of the elastic constants for the respective materials. In a recent study, we assessed the reliability of different exchange-correlation functionals and dynamical mean-field theory for the accurate prediction of the material properties of MAB phases [20]. We found that the PBE-GGA functional is sufficient to achieve a correct description of the energetics, structural, magnetic, and dynamical properties of M_2AB_2 , where $M = Fe$ and Mn , and $A = Al, Si, Ga,$ and In .

The temperature-dependent thermodynamic properties were calculated using the Phonopy software package [21–23]. Using this approach, the interatomic forces resulting from the displacement of atoms from their equilibrium sites were used to calculate the second-order force constants. A dynamical matrix was constructed to search for the phonon frequency distribution over the Brillouin zone. Supercells of size $4 \times 1 \times 4$ were used for MoAlB, WAIB, and Cr₂AlB₂ and size $4 \times 4 \times 2$ for Ti₂InB₂, respectively.

The harmonic approximation has serious inherent limitations including zero thermal expansion, temperature independence of elastic constants and bulk modulus, equality of constant-pressure and constant-volume specific heats, infinite thermal conductivity and phonon lifetimes, etc. In this respect, the quasiharmonic approximation provides the simplest route to overcome these limitations by incorporating explicit volume-dependent vibration phonon frequencies on the harmonic expression of the Helmholtz free energy.

Within this framework, the Helmholtz free energy, which relates the dependence of the vibration phonon frequency on volume, is expressed as the sum of three terms:

$$F(V, T) = U_0(V) + F_{\text{ph}}(V, T) + F_{\text{el}}(V, T). \quad (1)$$

Here $U_0(V)$ is the zero-temperature internal energy of the crystal without any vibrational contribution (easily accessible from the VASP via volume-constrained geometry optimizations). The second term $F_{\text{ph}}(V, T)$ is the vibrational contribution and can be expressed as

$$\begin{aligned} F_{\text{ph}}(V, T) &= \frac{1}{2} \sum_{q\sigma} \hbar\omega_{q\sigma} + k_B T \sum_{q\sigma} \ln(1 - \exp[-\hbar\omega_{q\sigma}/k_B T]), \end{aligned} \quad (2)$$

where $\omega_{q\sigma}$ is the vibrational frequency of the σ th branch with wavevector q . In this approach, the phonon frequency is dependent on the volume and independent of the temperature, hence the intrinsic phonon-phonon interaction which changes with temperature is neglected. Finally, the third term $F_{\text{el}}(V, T)$ is the electronic contribution to the free energy calculated from [24]

$$F_{\text{el}}(V, T) = E_{\text{el}} - TS_{\text{el}}, \quad (3)$$

where the electronic entropy is given by

$$S_{\text{el}} = -2k_B \sum_i \{f_i(V) \ln f_i(V) + [1 + f_i(V)] \ln [1 - f_i(V)]\}. \quad (4)$$

Here, the Fermi distribution function $f_i(V)$ is defined as

$$f_i(V) = \left\{ 1 + \exp \left[\frac{\varepsilon_i - \mu(V)}{T} \right] \right\}^{-1} \quad (5)$$

and E_{el} is

$$E_{\text{el}}(V) = 2 \sum_i f_i(V) \varepsilon_i(V). \quad (6)$$

The equilibrium volume at a given temperature T , $V(T)$, is obtained by minimizing $F(T, V)$ with respect to volume V , keeping T as a fixed parameter. Within this formalism, the total electron energy at $T = 0$ K and $p = 0$ and free vibrational energy F_{ph} were calculated for 13 volumes from -3.5% to 3.5% of the equilibrium unit-cell volume fitted to the Birch-Murnaghan equation of state. In these calculations, we applied strain independently along each direction and adjusted the lattice parameters in the transverse directions by modifying them according to isotropic Poisson's ratio.

III. RESULTS AND DISCUSSION

A. Structural properties

We present the relaxed crystal structures of the MoAlB, WAIB, Cr_2AlB_2 , and Ti_2InB_2 in Fig. 1. The structure of the MAB phase can be described as consisting of boron atoms coordinated by six transition-metal atoms. The MAB phase typically adopts the orthorhombic crystal structure, which comprises metal—boron (M—B) blocks made up of face-sharing trigonal prisms that are separated by layers of Al [25]. Recently, a hexagonal symmetry has been reported for Ti_2InB_2 with a space group of $P\bar{6}m2$ [7]. The structures considered in this investigation are based on experimentally synthesized MoAlB and WAIB with orthorhombic symmetry ($Cmcm$) [2], Cr_2AlB_2 with orthorhombic symmetry ($Cmmm$) [1], and Ti_2InB_2 with hexagonal symmetry ($P\bar{6}m2$) [7]. The direction of the zigzag B—B chain and

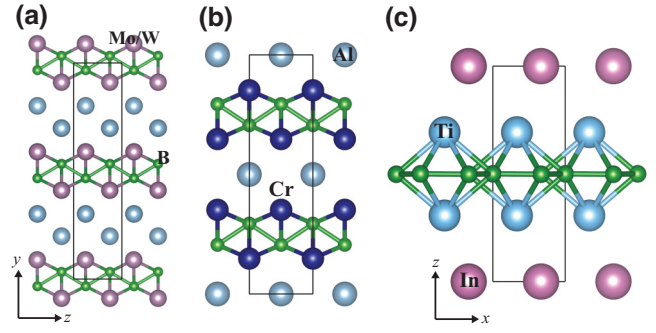


FIG. 1. Crystal structures of optimized (a) MoAlB and WAIB, (b) Cr_2AlB_2 , and (c) Ti_2InB_2 systems.

stacking direction for metal—boron layers for MoAlB, WAIB, and Cr_2AlB_2 are along the c and b lattice parameters, respectively. We set the c direction as the stacking direction for Ti_2InB_2 . The calculated lattice parameters and experimental values are summarized in Table I, showing a good agreement with experimental data, with deviations not more than 0.8% [1,2,7]. The largest deviation from the experimental results was obtained for the b lattice parameter, along which metal—boron layers are separated by Al layers.

B. Vibrational properties

We present the phonon dispersion curves and partial densities of states of the systems in Fig. 2. No negative frequencies, indicating the dynamical instability at $T = 0$ K, were found for all of the considered structures. The longitudinal acoustic and transverse acoustic modes of all the materials have a linear dependence as the phonon wave vector approaches zero (i.e., long-wavelength limit). For Ti_2InB_2 , this linear dependence continues until 2 THz. There are similarities in the behavior of systems with similar crystal structures, specifically for MoAlB and WAIB

TABLE I. Calculated lattice parameters (\AA) together with available experimental data.

	This calculation	Expt. [1,2,7,26]
MoAlB	$a = 3.22$	3.20
	$b = 14.03$	13.92
	$c = 3.11$	3.09
WAIB	$a = 3.22$	3.21
	$b = 13.98$	13.92
	$c = 3.12$	3.11
Cr_2AlB_2	$a = 2.93$	2.94
	$b = 11.13$	11.05
	$c = 2.92$	2.97
Ti_2InB_2	$a = 3.08$	3.10
	$b = 3.08$	3.10
	$c = 7.94$	7.71

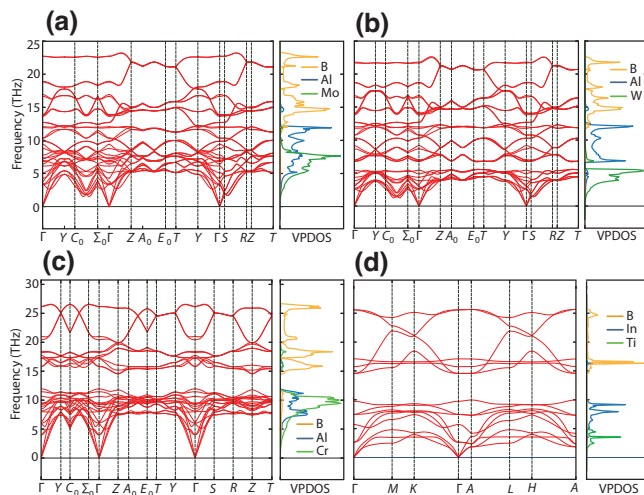


FIG. 2. Calculated phonon dispersion curve and vibrational phonon partial density of states (VPDOS) for (a) MoAlB, (b) WAIB, (c) Cr₂AlB₂, and (d) Ti₂InB₂.

[see Figs. 2(a) and 2(b)]. The low-frequency region up to 10–12 THz is predominantly dominated by the Mo—Al or W—Al vibrations and the high-frequency region is due to the B vibrational states. This behavior is attributed to the fact that the vibrational frequencies are inversely proportional to the mass of the atoms.

A comparison with the other two systems under investigation showed that the lower-frequency region is dominated by Cr—Al interactions and Ti—In, similar to the behavior described for MoAlB and WAIB. In contrast to the Mo- and Cr-based MAB phases, the Al and W vibrations are well separated. Though MoAlB has no phonon band gap, WAIB presents a phonon band gap of about 1 THz between low-lying optical phonons. Our density-of-states calculation for MoAlB is quite consistent with Raman spectra [27]. The largest band gap is exhibited by Ti₂InB₂, with a value of around 5 THz.

Since the phonon scattering depends on the number of available channels, which can be determined directly from the phonon dispersion plots, the existence of a phonon band gap provides the suppression of the scattering channels for phonons, thereby giving rise to longer mean free paths for phonons, and therefore higher lattice thermal conductivity. The maximum frequencies (ω_{\max}) at the Γ point exhibit the following order: $\omega_{\max}(\text{Cr}) > \omega_{\max}(\text{Ti}) > \omega_{\max}(\text{Mo}) > \omega_{\max}(\text{W})$. This ordering arises from the delicate interplay between the mass of the atoms and the stiffness of the bonds. It is noteworthy that the frequency (ω) is directly proportional to the bond stiffness and inversely proportional to the mass of the elements. Consequently, Ti and Cr, possessing smaller atomic masses, demonstrate higher values of ω_{\max} compared to Mo and W.

The investigated compounds display different dispersion curves, resulting in different phonon group velocities,

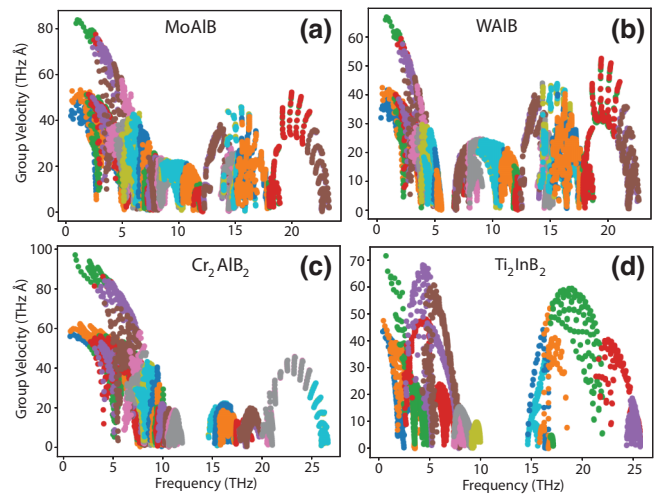


FIG. 3. Calculated phonon group velocities as a function of frequency. Each color represents a phonon branch in the respective systems.

$v_{q\sigma} = \partial\omega_{q\sigma}/\partial q$, where $\omega_{q\sigma}$, q , and σ represent the vibrational frequency, the phonon branch index, and the wave vector, respectively. From a comparison of the phonon group velocities as shown in Fig. 3, the acoustic modes take the largest values in Cr₂AlB₂, followed by MoAlB, Ti₂InB₂, and WAIB. On the other hand, Ti₂InB₂ exhibits consistently higher values of $v_{q\sigma}$ across the entire frequency spectrum, encompassing both acoustic and optical phonons, with the former generally making a larger contribution. MoAlB and WAIB exhibit very similar $v_{q\sigma}$ variations as a function of frequency. However, the latter generally has lower $v_{q\sigma}$ values. As the lattice thermal conductivity is directly related to the phonon group velocity and includes summation over phonon group velocities, it is expected that Cr₂AlB₂ and Ti₂InB₂ have larger thermal conductivities compared to MoAlB and WAIB. Figure 3 clearly demonstrates a significantly larger phonon band gap in Cr₂AlB₂ and Ti₂InB₂. This finding strongly supports the notion that these materials possess higher thermal conductivity.

Figure 4 denotes the Grüneisen parameters (γ) for MoAlB and Cr₂AlB₂. The γ parameter of an individual vibrational mode σ can be defined as $\gamma_{q\sigma} = -(V/\omega_{q\sigma})\partial\omega_{q\sigma}/\partial V$, and measures the rate of change of the phonon frequency $\omega_{q\sigma}$ with respect to the change in volume or lattice parameters due to an applied strain or thermal expansion. The Grüneisen parameter can be positive or negative. A negative Grüneisen parameter implies that the material's phonon frequencies decrease as the volume increases, and vice versa. In other words, the material's lattice vibrations become softer or more compressed under expansion and stiffer or more stretched under compression. This behavior is observed in some materials, particularly those with anharmonic lattice dynamics or specific structural characteristics.

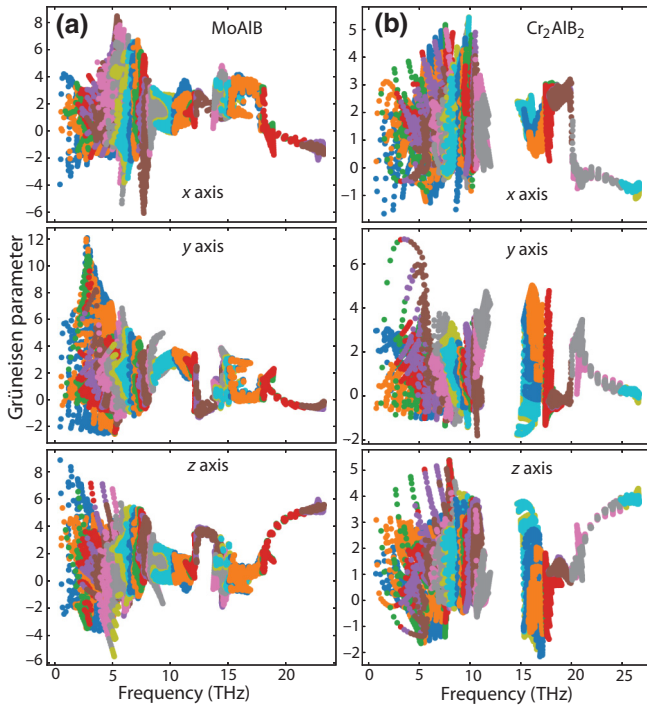


FIG. 4. The Grüneisen parameters corresponding to different phonon modes for (a) MoAlB and (b) Cr₂AlB₂ due to lattice expansion along only the x , y , and z directions.

We differentiated γ with respect to the lattice parameter change along the x (a), y (b), and z (c) directions. As seen from Fig. 4, the Grüneisen parameters strongly depend on the crystal direction. For instance, while γ varies between -2 and 12 along the y (or the lattice parameter b) direction, it ranges from -6 to 8 along the x and z directions for MoAlB. There is a sizable population of negative Grüneisen parameters in both materials, which is a sign of anharmonicity. However, this negative region is more dominant in MoAlB. As it is related to the thermal conductivity of a material through its effect on the lattice vibrations of the material, the Grüneisen parameter determines the anharmonicity of these vibrations, which in turn affects the scattering of phonons that carry heat through the material.

Upon examining MoAlB as a representative example up to 2.5 THz, distinct patterns emerge in the behavior of the transverse and longitudinal acoustic modes across different crystallographic directions. In the a and c directions, the frequencies of these modes decrease, while in the b direction, they increase. Notably, the a direction (along the x axis) displays more significant changes, characterized by larger negative Grüneisen parameters, as depicted in Fig. 4. Conversely, the c direction (along the z axis), which exhibits similar lattice parameters when expanded, shows comparatively smaller decreases in the transverse and longitudinal acoustic modes, aligning closely with the equilibrium structure. This observation is supported by

the Grüneisen parameters shown in Fig. 4, which indicate more negative values along the a direction than the c direction. In contrast, the b direction (along the y axis) demonstrates an increase in frequencies for both the longitudinal and transverse acoustic modes. This suggests a positive Grüneisen parameter that encompasses a broader range. As both the transverse and longitudinal modes experience an increase within the 0–2.5 THz range, the negative Grüneisen parameter is relatively lower in the b -axis graph of Fig. 4.

C. Thermal expansion

As a result of the potential of these materials in high-temperature applications, it is important to understand their thermal properties. The thermal properties of a material are part of the physical properties of the material and include heat capacity, thermal expansion, thermal conductivity, etc., which can provide information about the material's phase stability, strength, melting point, and bonding character [28]. Using the quasiharmonic approximation, we calculated changes in individual lattice parameters with temperature.

Figure 5 shows the calculated free-energy values for a range of temperatures obtained for MoAlB as a representative example. Free energy includes both electronic and vibrational contributions. Here, we differentiate the dependence of free energy along the lattice parameters a , b , and c . The red points mark the equilibrium lattice parameters, which minimize the free energy, at a given temperature. As is expected, the equilibrium lattice parameters grow with temperature, indicating the expansion of MoAlB in a given direction. Free-energy curves become flatter at large lattice constants above the equilibrium one as T grows.

To determine the thermal expansion properties along a specific direction (such as b lattice parameter), we employed a method that involved modifying the other orthogonal directions (a and c) using a positive isotropic Poisson's ratio. As illustrated in Fig. 1, MAB phases

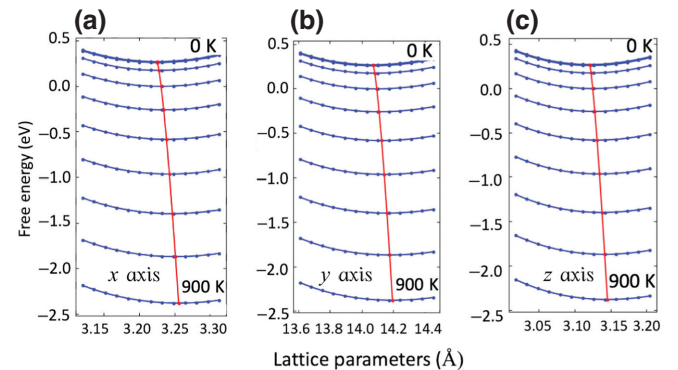


FIG. 5. Variation of free energy for MoAlB with respect to volume at temperatures 0–900 K along the x (or a), y (or b), and z (or c) directions.

exhibit highly anisotropic crystal structures, leading to direction-dependent mechanical properties. To validate our method, we conducted a comparison between the lattice parameters of MoAlB derived using an isotropic Poisson's ratio and those obtained through energy minimization. The optimized values for the a and c lattice parameters deviate by approximately 0.0062 and 0.0037 Å from the estimated values. These minimal differences in lattice parameters yield energy variations on the order of 0.5 meV. Consequently, our approach based on isotropic Poisson's ratio provides a reasonable estimation of the lattice parameters for orthogonal directions.

Figure 6 denotes the evolution of lattice parameters with temperature up to 1000 K. It shows that the unit-cell lattice parameters at temperatures up to 100 K are almost flat (or very small expansion compared to larger T values), then change rapidly to ascend linearly, as is consistent with experimental findings [8]. Our values for a , b , and c at 300 K are compared with data from the experiments where available. We obtained a , b , and c values higher than the experimental ones by 0.81%, 1.044%, and 0.64%, respectively, for MoAlB [1,8]. For Cr₂AlB₂ at 300 K, we obtained differences of 0.1%, 0.34%, and 1.18% for the a , b , and c lattice parameters, respectively. As various approximations (such as for treating exchange-correlation effects that have a significant impact on the lattice parameters) were used, a small discrepancy between experimental and computational lattice parameters is expected.

Therefore, it is more convenient to compare the slope of the experimental and calculated results. Both Cr₂AlB₂ and MoAlB exhibit fairly similar slopes in the linear part of their thermal expansion. However, above 500 K, the experimentally observed growth rate of the a lattice parameter (perpendicular to the B—B zigzag chain) becomes slightly

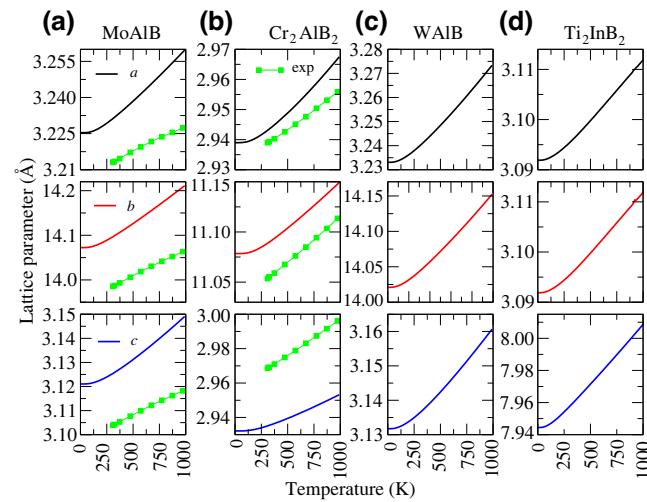


FIG. 6. Temperature dependence of equilibrium unit-cell lattice parameters. Green points are values obtained from the experiment [8].

slower. In general, we have a good agreement with the experimental results for the b and c lattice parameters, and the slope is steeper along these directions. When comparing our results with experimental data, it is evident that our method is well suited for accurately calculating the thermal expansion in MAB phases, as it aligns with the experimental data and captures the appropriate slope in the linear expansion region.

Next, we calculated the thermal expansion coefficient (TEC) for all systems under investigation. We achieved this by calculating the Helmholtz free energy at elevated temperatures for different lattice parameters. The obtained results are presented in Fig. 7 for temperature values 0–1000 K. At low temperatures, all materials behave in a similar way, with TEC increasing as the temperature increases up to about 500 K. Above 500 K, the effect of temperature on TEC is very small. Our calculated average linear expansion coefficients from low to high between 300 and 1000 K are $0.78 \times 10^{-5} \text{ K}^{-1}$ for Ti₂InB₂, $1.12 \times 10^{-5} \text{ K}^{-1}$ for Cr₂AlB₂, $1.15 \times 10^{-5} \text{ K}^{-1}$ for WAIB, and $1.18 \times 10^{-5} \text{ K}^{-1}$ for MoAlB. We found an agreement in the obtained values with previous experiments for MoAlB, where $0.95 \times 10^{-5} \text{ K}^{-1}$ and $1.05 \times 10^{-5} \text{ K}^{-1}$ were reported [29], and Cr₂AlB₂ [8], respectively. As far as we know, there are no experimental values for WAIB and Ti₂InB₂. Nevertheless, we expect a similar behavior between MoAlB and WAIB due to their identical crystal structures and the chemical similarities between Mo and W elements.

The average linear thermal expansions along the three principal axes (a , b , and c) are $1.25 \times 10^{-5} \text{ K}^{-1}$, $1.10 \times 10^{-5} \text{ K}^{-1}$, and $1.10 \times 10^{-5} \text{ K}^{-1}$ for MoAlB, and $0.87 \times 10^{-5} \text{ K}^{-1}$, $0.90 \times 10^{-5} \text{ K}^{-1}$, and $1.29 \times 10^{-5} \text{ K}^{-1}$ for Cr₂AlB₂. The order of the TEC values for MoAlB contradicts that of the experiment, where the a direction (perpendicular to the B—B chain) has the lowest average

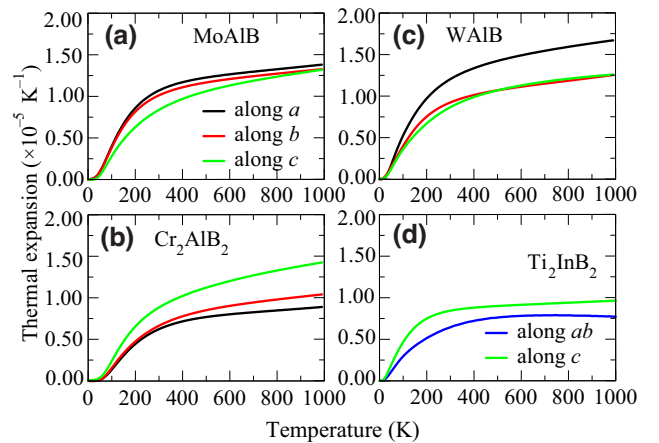


FIG. 7. Temperature dependence of thermal expansion coefficient for the MAB phases.

TEC value, followed by the c direction (parallel to the B—B chain) and the b direction (parallel to the stacking direction of the metal—boride units) [8]. Considering the small differences between the TEC values for different crystal directions, the computational parameters likely play a role in these results. We obtained $1.45 \times 10^{-5} \text{ K}^{-1}$, $1.0 \times 10^{-5} \text{ K}^{-1}$, and $1.1 \times 10^{-5} \text{ K}^{-1}$ for WAIB, and $0.67 \times 10^{-5} \text{ K}^{-1}$ and $0.81 \times 10^{-5} \text{ K}^{-1}$ for Ti_2InB_2 . These values suggest a varying degree of anisotropy in different systems, as the TEC values depend on the crystallographic direction in line with experiment [8].

In order to quantify how the TEC depends on the axis, we calculated the degree of anisotropy as

$$\alpha_{\text{anisotropy}} = \frac{\alpha_{\text{max}} - \alpha_{\text{min}}}{\alpha_{\text{ave}}} \times 100, \quad (7)$$

where α_{ave} is the average values along a , b , and c . Of all the systems studied, MoAIB is the most isotropic (having 13% anisotropy) consistent with experiment [8], followed closely by Ti_2InB_2 (17%). The highest degree of anisotropy is calculated for Cr_2AlB_2 (44%) followed by WAIB with a value of 30%. The result of the TEC confirms a significant difference in bonding in the different MAB phases despite the similarity in structural and chemical properties. Moreover, it has been suggested that the TEC is sensitive to the crystallographic direction [8]. Even though negative Grüneisen parameters (a sign of negative thermal expansion coefficient) were obtained, we did not find any negative TEC values for all systems.

D. Mechanical properties

1. Elastic constants

Understanding the mechanical properties of a material involves having insight into the elastic constants and moduli of the system. In order to investigate the elastic properties, the full set of independent second-order elastic coefficients was calculated. Elastic response (elasticity), which is related to the mechanical properties of a material, can be defined as the reaction of the material to an external force. There exist certain amounts of independent elastic constants, depending on the point-group symmetry of the crystals. For a system crystallizing in an orthorhombic (hexagonal) symmetry, there are nine (six) independent

coefficients [30–33]. We present the calculated elastic constants (C_{ij}) in Table II. Our obtained values are in good agreement with previous studies [2,31].

The calculated elastic stiffness constants show that the C_{ii} (i.e., elastic constants along the principal symmetry axes) are higher than all of the other combinations for all systems. Specifically, C_{11} , C_{22} , and C_{33} are larger than the shear elastic modulus, suggesting that the MAB phases show more resistance to a linear deformation along the a , b , and c axes. For MoAIB and WAIB, C_{22} is smaller than the corresponding C_{11} and C_{33} , implying that the system is more compressible along the b axis (or stacking direction). A similar observation is also valid for Cr_2AlB_2 . The largest elastic constant is C_{11} , which measures resistance to linear deformations along the direction perpendicular to the B—B zigzag chain running along the c direction. For WAIB, C_{11} and C_{22} are quite close. MoAIB has a more anisotropic elastic response as compared to WAIB. Considering the principal symmetry axes, Ti_2AlB_2 is more compressible along the c axis, which is perpendicular to the hexagonal B plane.

We can see that C_{12} , C_{13} , and C_{23} , which are the shear elastic constants, are quite close to each other for all cases we have reported. The elastic constants, C_{12} and C_{13} , calculate the stress component in the a direction with a uniaxial strain applied along the b and c direction, respectively. The larger value of the elastic component C_{13} implies that MAIB resists the shear along the c axis when an external force is applied along the crystallographic a axis. For Ti_2InB_2 , C_{12} and C_{13} (also C_{23} due to symmetry) are almost equal, and hence all axes are prone to similar responses.

Among the three shear components C_{23} has the highest value for WAIB followed by MoAIB and Cr_2AlB_2 . It combines a uniaxial strain along the c direction to stress along the b direction. The elastic constant C_{44} is connected with the indentation hardness of materials. Thus C_{44} indicates the material's ability to resist the shear deformation in the (100) plane and C_{66} reflects the resistance to shear in the [110] direction. The highest C_{44} and C_{66} values are computed for MoAIB and WAIB. The lowest value of Ti_2InB_2 indicates that it is more prone to deformation under external pressure.

Mechanical stability can be verified by checking the Born-Huang criterion [34]. The full expressions of the criterion for an orthorhombic structure are expressed

TABLE II. Calculated second-order elastic stiffness constants (GPa).

Compound	C_{11}	C_{12}	C_{13}	C_{22}	C_{23}	C_{33}	C_{44}	C_{55}	C_{66}
MoAIB	342.26	138.33	153.98	320.65	131.70	387.19	190.18	159.94	170.27
Cr_2AlB_2	451.40	113.19	117.29	422.42	104.59	522.82	161.64	216.28	164.30
WAIB	357.69	154.07	180.15	357.28	141.65	393.85	197.37	169.94	180.21
Ti_2InB_2	352.68	60.90	59.10	352.68	59.10	269.33	90.44	90.44	145.39

as: (i) $C_{11} > 0$, (ii) $C_{11}C_{22} > C_{12}^2$, (iii) $C_{11}C_{22}C_{33} + 2C_{12}C_{13}C_{23} - C_{11}C_{23}^2 - C_{22}C_{13}^2 - C_{33}C_{12}^2 > 0$, (iv) $C_{44} > 0$, (v) $C_{55} > 0$, and (vi) $C_{66} > 0$. Similarly, a mechanically stable hexagonal structure satisfies the following relations between the elastic constants: (i) $C_{11} > |C_{12}|$, (ii) $2C_{13}^2 < C_{33}(C_{11} + C_{12})$, and (iii) $C_{44} > 0$. We found that the calculated elastic constants satisfy the above conditions, indicating that all structures are mechanically stable structures.

2. Bulk and shear moduli

For orthorhombic systems, the Cauchy pressure, used to characterize the chemical bonding in a solid [35], can be defined for the three crystal directions as $P_a = C_{23} - C_{44}$, $P_b = C_{13} - C_{55}$, and $P_c = C_{12} - C_{66}$ [36–38]. A positive value signifies metallic bonding while a negative value connotes covalent bonding character. The calculated P_a values range between -58.5 and -55.7 GPa for the considered materials. Similarly, the P_c values vary between -51.1 and -26.1 GPa. We obtained the largest difference for P_b between MoAlB or WAIB and Cr₂AlB₂. The P_b value is found to be -98.9 GPa for Cr₂AlB₂. However, MoAlB and WAIB have values of -5.96 and 10.2 GPa, respectively. As a result of their large negative values of P_a and P_c , MoAlB, WAIB, and Cr₂AlB₂ exhibit significant directionality in their covalent bonds along the x and z directions. A negative Cauchy pressure also corresponds to brittleness. Hence all the ternary borides reported here are brittle in nature.

We also calculated the bulk modulus B , shear modulus G , Young's modulus E , and Poisson's ratio ν for each of the systems; the values obtained are summarized in Table III. The Young's modulus E was evaluated by utilizing the Voigt-Reuss-Hill (VRH) approximation method, where anisotropic single-crystal elastic constants can be converted into isotropic polycrystalline elastic moduli via the following expression [39]:

$$E = \frac{9B_{\text{VRH}}G_{\text{VRH}}}{3B_{\text{VRH}} + G_{\text{VRH}}}. \quad (8)$$

In this approach, the effective bulk modulus for polycrystals (B_{VRH}) and the shear modulus (G_{VRH}) become $B_{\text{VRH}} = \frac{1}{2}(B_V + B_R)$ and $G_{\text{VRH}} = \frac{1}{2}(G_V + G_R)$. Here, B_V , B_R , and

G_V , G_R are the Voigt and Reuss values for the bulk and shear moduli, respectively. According to Hill, based on energy considerations, the Voigt and Reuss equations set the upper and lower limits of realistic polycrystalline constants. Therefore, it is practical to estimate the bulk and shear moduli as the average of the Voigt and Reuss values.

While the bulk modulus measures the capability of a material to resist compression against forces applied to all sides, the shear modulus quantifies its resistance to a shape change or a plastic deformation. Our first observation is that the differences between B_V and B_R , and between G_V and G_R , are found to be small. Those differences may be used to measure the degree of elastic anisotropy in the MAB materials. From Table III, it is obvious that the bulk modulus increases as Ti₂InB₂ → MoAlB → Cr₂AlB₂ → WAIB. However, this trend is not completely valid for the shear modulus, such that Cr₂AlB₂ and Ti₂InB₂ possess the highest and lowest G values, respectively. This implies that Ti₂InB₂ exhibits the weakest resistance to shear deformation among the considered materials. However, all MAB materials overall have large shear modulus values, which is an indication of the more pronounced directional bonding between atoms.

As the size of the bulk modulus correlates with the nature and strength of the chemical bonds in solids, the comparatively high bulk modulus values of MoAlB, WAIB, and Cr₂AlB₂ indicate their ability to withstand volume deformation. Mechanical failure of a material is typically classified into two types as follows: brittle failure (i.e., fracture) and ductile failure (i.e., plastic deformation). A measure of the ductility of a material is Pugh's ratio of shear modulus to bulk modulus. The critical value of the ratio $B_{\text{VRH}}/G_{\text{VRH}}$ is about 1.75, indicating that materials with $B_{\text{VRH}}/G_{\text{VRH}} > 1.75$ are ductile, whereas those with $B_{\text{VRH}}/G_{\text{VRH}} < 1.75$ are brittle. We obtained $B_{\text{VRH}}/G_{\text{VRH}}$ values of 1.49, 1.29, 1.57, and 1.27 for MoAlB, Cr₂AlB₂, WAIB, and Ti₂InB₂, respectively. These values imply that Ti₂InB₂ (WAIB) is the most (least) brittle material. Note that all ternary borides considered here are brittle in nature.

Another indicator of the strength of the material is Young's modulus (E), which measures a material's resistance to longitudinal stress. The higher the E of the material, the stiffer it is. We present the E values (i.e., E_{VRH}) in Table III, from which it can be deduced that Cr₂AlB₂

TABLE III. Average mechanical properties of bulk polycrystalline MAB phases: bulk modulus B_R (Reuss), B_V (Voigt), and B_H (Hill) in GPa; shear modulus G_R (Reuss), G_V (Voigt), and G_H (Hill) in GPa; Pugh's ratio $B_{\text{VRH}}/G_{\text{VRH}}$, Poisson's ratio ν , and Young's modulus E in GPa.

Compounds	B_R	B_V	B_H	G_R	G_V	G_H	$B_{\text{VRH}}/G_{\text{VRH}}$	ν	E
MoAlB	209.20	210.90	210.05	136.05	145.82	140.93	1.49	0.23	345.53
Cr ₂ AlB ₂	228.24	229.64	228.94	176.42	179.22	177.82	1.29	0.19	423.74
WAIB	228.02	228.95	228.48	139.92	151.69	145.80	1.57	0.24	360.69
Ti ₂ InB ₂	145.68	147.88	146.78	112.64	118.16	115.40	1.27	0.19	274.31

is the stiffest and Ti_2InB_2 the least stiff of the materials considered. We may classify MoAlB , Cr_2AlB_2 , and WAIB as stiff materials owing to their Young's modulus being larger than 345 GPa. While experimental values of C_{ij} are not available, we compared our obtained E and G values with data from experiment where available [11,40]. In particular, our obtained E_{VRH} and G_{VRH} values of 345.53 and 140, respectively, for MoAlB are about 7.3% lower than the values of 373 and 151 obtained by Kota *et al.* [40]. Our E_{VRH} and G_{VRH} values for MoAlB and Cr_2AlB_2 are larger than those of MAX phases (layered hexagonal ternary carbides and nitrides, where M is an early transition metal, A is a group A element, and X is carbon or nitrogen) such as Ti_2AlC and Ti_3AlC_2 [2]. Overall the elastic properties reflect the behavior previously reported experimentally.

Next, we evaluated Poisson's ratio (ν) using the following expression:

$$\nu = \frac{3B_{\text{VRH}} - 2G_{\text{VRH}}}{2(3B_{\text{VRH}} + G_{\text{VRH}})}. \quad (9)$$

It is a key quantity for assessing a material's stability against shear. Poisson's ratio takes values in the range from -1 to 0.5 dictated by the positivity requirement of the stiffness for a stable material. With values lower than 0.26 , a material is brittle; otherwise the material is ductile. The observed trend here is in agreement with Pugh's ratio described above. Poisson's ratio can be utilized to characterize the type of chemical bonding in solids. Typically, a Poisson's ratio as small as 0.1 implies covalent bonding, whereas metallic materials have a Poisson's ratio value greater than 0.33 . A low Poisson's ratio indicates a stronger degree of covalent bonding that gives rise to a higher hardness. Our calculated Poisson's ratio values fall into a range of 0.19 to 0.24 , which indicates a mixture of covalent, metallic, and ionic interatomic bonding. Based on Table III, the degree of covalent character is strongest in Ti_2InB_2 , which may be due to the B—B hexagonal lattice.

3. Mechanical anisotropy

Because of the crystal symmetry and different chemical bonding along different crystal directions, an anisotropic behavior in mechanical properties must be expected. Elastic anisotropy is a major precursor for microcracks found in solids, and hence it is a topic of interest in the description of the mechanical properties of systems. One approach to demonstrate elastic anisotropy in materials is the construction of mechanical moduli as a function of direction.

To measure the anisotropy in mechanical properties, we calculated various metrics. Among them, the shear anisotropy factors can be correlated with the anisotropy in bonding between atoms [41]. The shear anisotropy factors for an orthorhombic crystal can be expressed as

follows [41,42]:

$$A_1 = \frac{4C_{44}}{C_{11} + C_{33} - 2C_{13}} \quad (10)$$

for the (100) shear planes between the [011] and [010] directions,

$$A_2 = \frac{4C_{55}}{C_{22} + C_{33} - 2C_{23}} \quad (11)$$

for the (010) shear planes between the [101] and [001] directions, and

$$A_3 = \frac{4C_{66}}{C_{11} + C_{22} - 2C_{12}} \quad (12)$$

for the (001) shear planes between the [011] and [010] directions.

Similarly, for hexagonal Ti_2InB_2 , three shear anisotropy factors involving elastic constants can be expressed via [43]

$$A_1 = \frac{C_{11} + C_{12} + 2C_{33} - 4C_{13}}{6C_{44}}, \quad (13)$$

$$A_2 = \frac{2C_{44}}{C_{11} - C_{12}}, \quad (14)$$

$$A_3 = \frac{C_{11} + C_{12} + 2C_{33} - 4C_{13}}{3(C_{11} - C_{12})}. \quad (15)$$

The values obtained from Eqs. (10)–(15) are summarized in Table IV. A deviation from unity connotes elastic anisotropy. From the values in Table IV, we can deduce that the studied borides are elastically anisotropic. Also observed is the significant difference in the in-plane (along the transition-metal boride layer) and out-of-plane (perpendicular to transition-metal boride layer) interatomic interactions.

Furthermore, elastic anisotropy can be measured as percentage anisotropy in compressibility and shear. The

TABLE IV. Calculated shear anisotropy factors A_1 , A_2 , and A_3 , and percentage anisotropy factors A_B and A_G . In the last column, A_u is the universal anisotropy index.

Compound	A_1	A_2	A_3	A_B (%)	A_G (%)	A_u
MoAlB	1.62	1.44	1.97	0.41	3.46	0.37
Cr_2AlB_2	0.87	1.17	1.02	0.31	0.79	0.09
WAIB	1.84	1.45	1.94	0.20	4.04	0.42
Ti_2InB_2	1.32	0.62	0.82	0.75	2.39	0.26

approach involves evaluating

$$A_B = \frac{B_V - B_R}{B_V + B_R} \times 100\%, \quad (16)$$

$$A_G = \frac{G_V - G_R}{C_V + G_R} \times 100\%, \quad (17)$$

where B and G indicate the bulk and shear moduli and their subscripts V and R represent the Voigt and Reuss limits, respectively. When $B_R = B_V$ and $G_R = G_V$, then both A_B and A_G become zero, which corresponds to a completely isotropic material. Again, the values presented in Table IV indicate that all the MAB materials reported here are highly anisotropic in compression as compared to shear. The least anisotropic material in both compression and shear is Cr_2AlB_2 .

We also calculated the universal anisotropy index [44]:

$$A_u = 5 \frac{G_V}{G_R} + \frac{B_V}{B_R} - 6. \quad (18)$$

The value of A_u is zero for locally isotropic single crystals. The departure from zero quantifies the extent of anisotropy and accounts for both compressibility and shear contributions. The highest and lowest values of A_u are shown by Cr_2AlB_2 and WAIB, respectively, which indicates that the former and latter are the least and most anisotropic, respectively.

4. Hardness

The hardness of a material is its ability to resist plastic deformation when a load is applied to it. Even though DFT is a powerful tool to compute various mechanical properties, including elastic constants, bulk, shear, and Young's moduli, and Poisson's ratio, a direct prediction of hardness via first-principles calculations is challenging and strongly correlates with the material type and properties. Therefore, various semiempirical relations (labeled as H_i , where $i = 1a, 1b, 2, 3, 4, 5, 6$ and 7) have been proposed to estimate hardness utilizing commonly known elastic properties, such as bulk modulus B , shear modulus G , Young's modulus E , and Poisson's ratio ν [47]. These models include: $H_{1a} = 0.1475G$ [48], $H_{1b} = 0.0607E$

[48], $H_2 = 0.1769G - 2.899$ [49], $H_3 = 0.0635E$ [50], $H_4 = (1 - 2\nu)B/(6(1 + \nu))$ [51], $H_5 = 2(G^3/B^2)^{0.585} - 3$ [52], and $H_6 = \gamma_0\chi(\nu)E$ [53]. Note that H_{1a} and H_{1b} share similar mathematical forms, but their expressions vary based on the different mechanical constant used in the calculations. In the last hardness expression (H_6), $\chi(\nu) = (1 - 8.5\nu + 19.5\nu^2)/(1 - 7.5\nu + 12.2\nu^2 + 19.6\nu^3)$ and $\gamma_0 = 0.096$. Yet another expression, $H_7 = 740(P - P')v_b^{-5/3}$, involves the volume of the bond (v_b), Milliken bond population (P), and metallic population ($P' = n_{\text{free}}/V$) to take into account the metallicity of partial metallic bonds [54]. Here, $n_{\text{free}} = \int_{E_F}^{E_F} N(E) dE$, where $N(E)$ is the density of states (DOS) and E_F is the Fermi level.

Table V lists computed hardness values from these methods together with available experimental data. Hardness relations from H_{1a} to H_5 overestimate the hardness of MoAlB and Cr_2AlB_2 . However, we obtained a very good agreement with experiment for WAIB. These results imply that the models up to H_6 , combining various mechanical quantities, are incapable of predicting the hardness of all MAB phases considered here. According to a recent work, H_{1a} works well for cubic metallic systems, whereas H_{1b} is good for hexagonal insulators [55]. Model H_4 is the best for metals with any crystal symmetry. Among the models between H_{1a} and H_6 , we obtained one of the best performances from H_4 for MoAlB, Cr_2AlB_2 , and WAIB.

Model H_7 , based on a detailed analysis of chemical bonds, exhibits the best performance for most of the MAB phases. The calculated hardness values of MoAlB and Cr_2AlB_2 agree well with experiment. Generally, the hardness of MAB phases is significantly lower than those of transition-metal mono- and diborides due to their nanolaminated structures. Even though all known superhard materials exhibit high bulk moduli, possessing high incompressibility does not necessarily translate into high hardness. For instance, while diamond and osmium are both ultracompressible, diamond is significantly harder than osmium [56]. Similarly, in spite of having the largest bulk moduli among the considered MAB phases, Cr_2AlB_2 has a remarkably low hardness as compared to MoAlB and WAIB. The resistance to plane slippage and dislocation motion directly affects the hardness.

TABLE V. Vickers hardness values (GPa) of MAB compounds calculated with various relations, together with experimental measurements.

Compounds	H_{1a}	H_{1b}	H_2	H_3	H_4	H_5	H_6	H_7	H_{exp}
MoAlB	20.8	20.9	22.0	21.9	15.4	19.7	15.9	11.5	11.4–13.6 [1] 10.3 [45]
Cr_2AlB_2	26.2	25.7	28.6	26.9	19.9	27.8	24.1	7.0	6–7 [1] 10.4 [46]
WAIB	21.5	21.9	22.9	22.9	15.9	18.8	16.6	8.6	21.7 [1]
Ti_2InB_2	17.0	16.6	17.5	17.4	12.7	21.3	15.6	2.5	...

Low-temperature constant-pressure specific heat measurements found that Cr_2AlB_2 has about four times larger electronic density of states at the Fermi level than MoAlB, which implies that the former is a better conductor. The presence of enhanced metallicity may result in Cr_2AlB_2 being much more susceptible to slip, thereby a lower hardness. By solely considering the calculated mechanical constants, as in the case of MoB and WB, one would expect MoAlB and WAIB to have similar hardness values [1,45]. However, the experimental measurements revealed that the latter has about two times larger Vickers hardness value. Also, the experimental hardness values of WB are between 20.8 and 26.7 GPa, being very close to that of WAIB. Though MoAlB and Cr_2AlB_2 exhibit about 53% and 64% lower hardness values, respectively, as compared to their parent metal borides, WAIB only has a 20% reduction with respect to WB. Unfortunately, the H_7 model significantly underestimates the hardness of WAIB.

To gain insight into the nature of chemical bonding in MAB phases and its relationship to hardness, we calculated: (i) Bader and Mulliken charges (which provide a quantitative estimation for the extent of charge transfer between atoms); (ii) the density of states at the Fermi level; and (iii) the crystal orbital Hamilton population (COHP). The first two quantities (i) and (ii) will be used to assess the ionic bonding and metallicity. On the other hand, the integrated COHP (ICOHP) mainly measures the strength of the covalency of a bond. A larger $-\text{ICOHP}$ value corresponds to a stronger covalent bond. The calculated Bader and Mulliken charges indicate a significant electron transfer from metal atoms to B atoms in all cases. The Al atoms donate electrons and are therefore positively charged. Hence, there is also an ionic contribution to the bond of these atoms. In Ti_2InB_2 , In and B atoms receive charge from the Ti atoms. All compounds exhibit different degrees of ionic bonding that contributes to the hardness and brittle nature of the MAB phases considered. The greater the polarity of the M—B bond, the stronger the ionic bond is.

The density of states at the Fermi level ($N(E_F)$) is 0.92, 2.50, 0.51, and 1.44 (eV f.u.^{-1}) (f.u. = formula unit) for MoAlB, Cr_2AlB_2 , WAIB, and Ti_2InB_2 , respectively. Our results for MoAlB and Cr_2AlB_2 are about 50% of the experimental values obtained from the low-temperature specific-heat measurements via $3\gamma_{\text{cp}}/((1 + \lambda)\pi^2k_B^2)$, where electron-phonon coupling ($\lambda = 0$) was not included, which could imply the presence of a non-negligible role of electron-phonon coupling in the MAB phases [2]. In this equation, γ_{cp} is the experimentally measured electronic coefficient of heat capacity. In this respect, we calculated the electron-phonon coupling parameter λ for Cr_2AlB_2 . We found that the λ value is around 0.12 [57]. In an unpublished work, we obtained a much larger λ value ($= 0.6$) for Tc_2AlB_2 in a Cr_2AlB_2 -type crystal structure. The larger atomic masses of transition

metals in comparison to Cr result in WAIB and MoAlB having λ values of 0.14 and 0.18, respectively. This difference in λ values could potentially impact the experimental density of states at the Fermi energy ($N(E_F)$). Having a low λ value verifies that Cr_2AlB_2 is a better conductor compared to WAIB and MoAlB.

As high electrical conductivity is generally correlated with the density of states at the Fermi level, Cr_2AlB_2 and Ti_2InB_2 have higher electrical conductivity values than MoAlB and WAIB. WAIB has the lowest $N(E_F)$ and is expected to have the lowest metallic bonding contribution, thereby lowest hardness weakening due to metallic bonding. In fact, a lower resistivity was observed in Cr-doped MoAlB as compared to W-doped one [2], providing indirect support for our results. Among the considered MAB phases, the existence of weakest metallicity in WAIB may be the one of the factors that results in a high hardness and signifies why hardness models H_{1a} to H_3 work well for this compound.

In the COHP analysis, we split the band-structure energy into bonding, nonbonding, and antibonding contributions using localized atomic basis sets. The energy integration of all COHP for a pair of atoms up to the Fermi energy (ICOHP) can be used to qualify bond strength [58]. The Local Orbital Basis Suite Towards Electronic-Structure Reconstruction (LOBSTER) code is utilized for the COHP calculations with the pbeVaspFit2015 basis set [59–61]. The B—B bonds have large values of the COHP function for all borides considered, meaning a strong covalent bonding. The average of $-\text{ICOHP}$ for B—B is 6.04 eV for WAIB, 5.69 eV for MoAlB, and 4.80 eV for Cr_2AlB_2 . The M—Al and B—Al bonds are stronger in WAIB followed by MoAlB and Cr_2AlB_2 . The M—B bond strengths are quite similar in WAIB, MoAlB, and Cr_2AlB_2 .

In general, most of the interactions are stronger in WAIB and MoAlB than in Cr_2AlB_2 and Ti_2InB_2 , providing an explanation as to why Cr_2AlB_2 has a lower hardness value measured experimentally. Also, our COHP analysis suggests that it is easier to delaminate Cr_2AlB_2 , in line with experiments. The M—M bonds have much lower values of COHP, and hence reduced bond strength due to a reduced wave-function overlap between orbitals centered on these atoms. As evident from Table V, experimentally, WAIB has the highest Vickers hardness, indicating that it is hard to be deformed. But all the materials listed above have hardness values much lower than 40 GPa, which means that they are not superhard materials [62].

The fracture toughness K_{IC} of a material is its resistance to crack propagation and is one of the most important mechanical properties of materials. Similar to hardness, theoretical modeling of fracture toughness is challenging. MAB phases exhibit metallic properties and bonding that should be incorporated into fracture toughness prediction, as the fracture toughness of metals is usually one or two orders higher than that of ionic or covalent crystals. This

can be attributed to the lower crack sensitivity of metallic bonding compared with ionic and covalent bonds, since the former can be easily broken and reformed.

We first adapted the following simple approach by combining shear modulus and Pugh modulus to calculate the fracture toughness [67]:

$$K_{IC} = V_0^{1/6} G_{VRH} (B_{VRH}/G_{VRH})^{1/2}, \quad (19)$$

where V_0 is the volume per atom (m^3). A solid with a large K_{IC} means high resistance to crack propagation. In spite of its simplicity, our calculated K_{IC} value for MoAlB is only 14.7% smaller than the experimental ones. Except for Ti_2InB_2 , the other MAB phases have similar K_{IC} values. Equation (19) accounts only for covalent and ionic crystals. As the MAB phases exhibit metallic properties and possess metallic bonding to some extent, we need to incorporate that metallicity.

Thus, an enhancement factor α is added to Eq. (19) to obtain a new expression for intermetallic solids (composed of two or more elements with metallic bonding) [68]:

$$K_{IC} = \alpha V_0^{1/6} G_{VRH} (B_{VRH}/G_{VRH})^{1/2}, \quad (20)$$

where α reflects the degree of metallicity. It was set equal to $\alpha = 43g(E_F)_R^{1/4} f_{EN}$. Here, f_{EN} is the electronegativity factor, which depends on the Allen-scale electronegativity of the elements and includes various parameters that can be obtained by fitting it to experimental results. Also here, $g(E_F)_R$ is the relative DOS at the Fermi level and is given by $g(E_F)_R = g(E_F)/g(E_F)_{FEG}$, where $g(E_F)_{FEG}$ is the DOS for a free-electron gas. Because of the absence of enough experimental data, we are unable to obtain α . Comparison of K_{IC} calculated via Eq. (19) with experiment implies that α is larger than 1 for MAB phases. For instance, it is equal to about 1.17 for MoAlB. The highest fracture toughness is shown by Cr_2AlB_2 , indicating that it has the highest tolerance to crack extension, followed by WAIB, MoAlB, and Ti_2AlB_2 .

E. Debye temperature

Debye temperature is an important quantity in the determination of many physical properties of a solid, such as melting temperature, specific heat, lattice vibration, thermal conductivity, and thermal expansion. The Debye temperature is calculated from the following equation using the average sound velocity [69]:

$$\theta_D = \frac{h}{k_B} \left[\left(\frac{3n}{4\pi} \right) \frac{N_A \rho}{M} \right]^{1/3} v_s, \quad (21)$$

where h is Planck's constant, k_B is Boltzmann's constant, N_A is Avogadro's number, ρ denotes mass density, M is the molecular weight, and n is the number of atoms in the

TABLE VI. Calculated density ρ (g/cm^3), longitudinal, transverse, and average sound velocities v_l , v_t , and v_s (km/s) and Debye temperature θ_D (K).

Compounds	ρ	v_l	v_t	v_s	θ_D
MoAlB	6.33	7.93	4.72	5.22	685
Cr_2AlB_2	5.35	9.33	5.76	6.36	895
WAIB	10.46	6.36	3.73	4.14	542
Ti_2InB_2	5.90	7.14	4.42	4.88	616

unit cell. The average sound velocity v_s in polycrystalline solids is governed by [70]

$$v_s = \left[\frac{1}{3} \left(\frac{1}{v_l^3} + \frac{2}{v_t^3} \right) \right]^{-1/3}, \quad (22)$$

where v_l and v_t are the longitudinal and transverse sound velocities in the polycrystalline material. These obtained using the polycrystalline shear modulus G_{VRH} and the bulk modulus B_{VRH} using the following equations [70]:

$$v_l = \left[\frac{3B_{VRH} + 4G_{VRH}}{3\rho} \right]^{1/2} \quad (23)$$

and

$$v_t = \left[\frac{G_{VRH}}{\rho} \right]^{1/2}. \quad (24)$$

The calculated Debye temperature θ_D along with sound velocities v_l , v_t , and v_s are presented in Table VI. A higher Debye temperature is associated with a higher phonon thermal conductivity. This is attributed to the fact that the Debye temperature is the temperature above which all phonon modes are assumed to be excited, thereby giving rise to enhanced phonon-phonon scattering. The calculated Debye temperature as well as the sound velocities for Cr_2AlB_2 are higher than those for the rest of the studied systems under investigation. This implies that Cr_2AlB_2 is expected to be thermally more conductive than the other studied compounds. The calculated Debye temperature for MoAlB is in agreement with previous work [66].

F. Thermal conductivity

Slack suggested that thermal conductivity is governed by four factors: (1) average atomic mass, (2) interatomic bonding, (3) crystal structure, and (4) size of anharmonicity [71]. The first three factors describe the harmonic properties. The three-phonon scattering-dominated thermal conductivity κ_{ph} (i.e., $\sim 1/T$) can be described as

$$\kappa_{ph}^S = \frac{A_\gamma V M_{av} \theta_D^3}{\gamma^2 T n^{2/3}}. \quad (25)$$

Here V represents the volume per atom, M_{av} denotes the average atomic mass per atom, T represents the absolute

temperature, n is the number of atoms in the primitive cell, γ is the Grüneisen parameter, and A_γ is the influence factor dependent on γ . In this equation, the Grüneisen parameter is a measure of the degree of anharmonicity, such that the larger the Grüneisen parameter of the mode, the stronger the anharmonicity is. In other words, a larger anharmonicity means more frequent scattering of a phonon mode by other phonon modes. The γ and A_γ above are calculated using the following equations:

$$\gamma = \frac{3(1 + \nu)}{2(2 - 3\nu)}, \quad (26)$$

where ν is the Poisson's ratio, and

$$A_\gamma = \frac{2.436 \times 10^{-8}}{(1 - 0.514/\gamma + 0.228/\gamma^2)}. \quad (27)$$

In these expressions, we considered an isotropic Poisson's ratio, which does not reflect anisotropy in the respective systems.

We also computed the thermal conductivity using a modified Slack model utilizing no fitting parameter [65, 66, 72]. In this model, the contribution of optical phonons to total thermal conductivity is neglected. By utilizing the high-temperature limit for the heat capacity and assuming Umklapp scattering as the dominant scattering mechanism, the expression for the lattice thermal conductivity is as follows:

$$\kappa_{\text{ph}}^T = \frac{(6\pi)^{2/3}}{4\pi^2} \frac{M_{\text{av}} v_s^3}{TV^{2/3}\gamma^2} \frac{1}{n_D}. \quad (28)$$

Here v_s is the average speed of sound, n_D is the number of atoms per unit cell, M_{av} is the average atomic mass per formula unit, V is the volume per atom, and γ is the thermodynamic Grüneisen parameter given in Table VII. In Ref. [72], a dependence of $n_D^{-1/3}$ was employed for structurally complex materials. Here, we adopted the use of n_D^{-1} , which provides a good fit to experimental results. Utilizing $n_D^{-1/3}$ leads to thermal conductivity values that are even higher than those predicted by the Slack model.

Table VII lists our calculated γ and A_γ values for the Slack model. One can argue that γ is strongly correlated

with the mass of the transition-metal atom. For instance, as the W atom is 3.84 times heavier than the Ti atom, WAIB has the largest Grüneisen parameter. Therefore, it is expected that the anharmonic effects should be strongest in WAIB. Figure 8 shows the calculated lattice thermal transport properties via the Slack model of all the studied compounds. It is evident that Cr_2AlB_2 has the highest thermal conductivity, due to it having the largest Debye temperature and relatively smaller Grüneisen parameter value, followed by Ti_2InB_2 , MoAlB, and WAIB. Also, as seen from Fig. 3, the phonon group velocities are overall larger in Cr_2AlB_2 and Ti_2InB_2 . As we increase temperature, the thermal conductivity decreases due to the enhanced phonon-phonon scattering via the Umklapp process as described by the $1/T$ dependence in the above equations.

When comparing experimental results for MoAlB, the Slack method (developed for nonmetallic solids) markedly overestimates the thermal conductivity values. The calculated κ_{ph} value at $T = 300$ K is around $34.8 \text{ W m}^{-1} \text{ K}^{-1}$ for MoAlB, which is far above the experimental value of around $6.33 \text{ W m}^{-1} \text{ K}^{-1}$ [65, 66]. Therefore, we attempted to calculate thermal conductivity using a modified model based on the Slack approach given in Eq. (28). As seen from Fig. 8, this modified model reduces thermal conductivity values substantially. Thus, the κ_{ph}^T values are now quite close to the experimental ones such that, at $T = 300$ K, the value decreases from $34.8 \text{ W m}^{-1} \text{ K}^{-1}$ (for κ_{ph}^S) to $9.49 \text{ W m}^{-1} \text{ K}^{-1}$ (for κ_{ph}^T). A $1/T$ dependence observed in experiment signifies the dominant role of the Umklapp process in phonon-phonon scattering, which is included in both models. Moreover, the slope of the calculated curves agrees well with the experimental one at all temperatures.

The Slack equation provides a cost-effective alternative to other expensive methodologies, including computing the anharmonic force constants or time-consuming *ab initio* molecular dynamics. However, its accuracy relies heavily on two variables: the acoustic Debye temperature, $\theta_a = n^{-1/3}\theta_D$, and the Grüneisen parameter, γ . Here, θ_D , calculated using the elastic properties, provides a characterization of the entire vibrational spectrum. The term $n^{-1/3}$ is utilized to roughly distinguish the acoustic branches from the overall vibrational spectrum. It is important to note that different definitions of these variables can be used,

TABLE VII. Definition of the parameters used in our work: K_{IC} , fracture toughness ($\text{MPa m}^{1/2}$); δ , average atomic volume; M_{av} , average atomic mass; γ , Grüneisen parameter; n , number of atoms in the unit cell; A_γ , numerical factor; κ_{ph}^t , calculated lattice thermal conductivity ($\text{W m}^{-1} \text{ K}^{-1}$) at 300 K; and $\kappa_{\text{ph}}^{\text{exp}}$, experimental lattice thermal conductivity ($\text{W m}^{-1} \text{ K}^{-1}$) at 300 K.

Compounds	K_{IC}	$K_{\text{IC}}^{\text{exp}}$	δ	M_{av}	γ	n	$A_\gamma \times 10^{-8}$	κ_{ph}^t	$\kappa_{\text{ph}}^{\text{exp}}$
MoAlB	3.92	4.3–4.9 [63, 64]	2.27	44.58	1.39	12	3.25	9.49	6.33 [65, 66]
Cr_2AlB_2	4.31		2.12	30.52	1.25	10	3.31	18.09	
WAIB	4.16		2.27	73.88	1.44	12	3.23	7.29	
Ti_2InB_2	2.61		2.36	46.43	1.24	5	3.31	23.53	

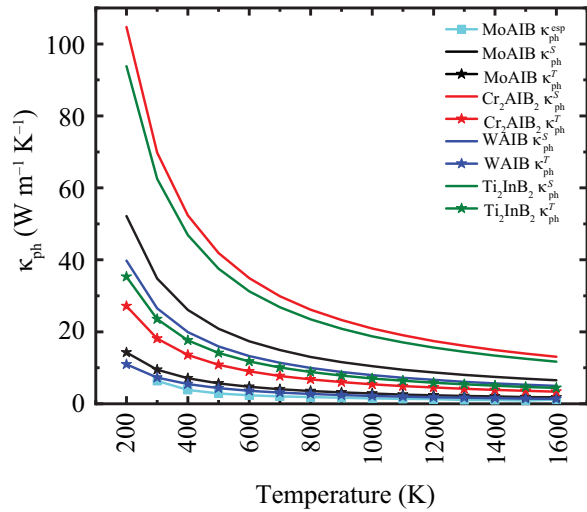


FIG. 8. Variation of thermal conductivity as a function of temperature calculated via Slack (κ_{ph}^S) and modified Slack (κ_{ph}^T) models. Experimental data are also plotted for MoAlB.

depending on the specific model or approximation being employed. To exemplify, when determining the Debye temperature, we employ v_s , which is derived from the average of the longitudinal and transverse speeds of sound. In addition, for a given Debye temperature and Grüneisen parameter, the overestimation of thermal conductivity in our work can be attributed to the A_γ parameter in the Slack model.

In a recent work, it was shown that an optimized Slack model incorporating a new A_γ parameter demonstrates a significantly improved agreement between the predicted κ value and the experimentally measured κ value, surpassing the accuracy of previous predictions [73]. Both models exhibit the same dependence on the Grüneisen parameter, and its determination was carried out in the same way. However, it should be noted that the modified model does not incorporate the parameter A_γ , which can introduce errors in predicting the thermal conductivity. In the Slack model, the thermal conductivity is dependent on $n^{-2/3}$, whereas in the modified model, it is governed by a dependence on n^{-1} . The latter leads to a more pronounced reduction in thermal conductivity, owing to this particular dependence.

The Grüneisen parameter and sound velocity likely account for the source of discrepancy between theory and experiment in the modified model. Moreover, since the impact of structural defects and high-order phonon-phonon scatterings are not included in the calculations, our values are larger than the experimental ones, as expected. Also, we did not include the phonon lifetimes, requiring third-order force-constant calculations, and the electronic contribution to the thermal conductivity. Nevertheless, the simple expression we used provides a surprisingly good prediction for thermal conductivity properties of the MAB

phases, which can be improved further by using more accurate Grüneisen parameter and sound velocity values. The calculated Grüneisen parameters shown in Fig. 4 suggest a large degree of anharmonicity and an anisotropic lattice thermal conductivity in MoAlB in line with experimental work where thermal transport is favored perpendicular to the basal planes (or stacking direction) in MoAlB [65,66].

Finally, we examined the contribution of optical phonons to thermal conductivity using the following expression [65,66,72]:

$$\kappa_o = \frac{3k_B v_s}{2V^{2/3}} \left(\frac{\pi}{6}\right)^{1/3} \left(1 - \frac{1}{n_D^{2/3}}\right). \quad (29)$$

We found that the contribution of optical phonons is about three orders of magnitude smaller compared to that of acoustic phonons. This suggests that acoustic phonons dominate the thermal conductivity in the system studied, while the influence of optical phonons is relatively negligible.

IV. CONCLUSION

A systematic investigation of the structural, vibrational, mechanical, and thermal properties of MoAlB, WAIB, Cr₂AlB₂, and Ti₂InB₂ was performed using a combination of density-functional theory (DFT) and the quasiharmonic approximation (QHA). The calculated evolution of structural parameters with temperature agrees well with experimental findings. Further analysis revealed a varying degree of thermal expansion coefficient (TEC) anisotropy. While a mild TEC anisotropy was found in MoAlB, Cr₂AlB₂ and WAIB possess the highest degree of TEC anisotropy, suggesting differences in bonding character in these systems despite structural similarities. Evaluation of the Cauchy pressure, and the Pugh's, and Poisson's ratios revealed that the systems are brittle. Determination of the Bader and Mulliken charges, density of states at the Fermi level, and the crystal orbital Hamilton population reveal a mixed chemical bonding, which governs the mechanical and thermal properties of MAB phases. Having a complex chemical bonding and lamellar structure complicates the description of hardness in this material family. Models considering Young's, bulk, and shear moduli or Poisson's ratio substantially overestimate the hardness values of MoAlB and Cr₂AlB₂. Interestingly, these models work well for WAIB. This may be due to enhanced covalent character and weak metallicity in this material.

The calculated electron-phonon coupling parameter (λ) for some MAB compounds indicated that λ ranges between 0.1 and 0.6, implying from weak to mild coupling depending on the material. Another method involving Mulliken bond population, metallic population, and density of states provides a very good estimation for MoAlB and Cr₂AlB₂. We found that simple empirical relations

combining Debye temperature, Grüneisen parameter, and sound velocity, and incorporating solely Umklapp process as the main phonon-phonon scattering mechanism, can well describe thermal conductivities in the MAB phases. Because of their lower Grüneisen parameters and larger sound velocities, Cr_2AlB_2 and Ti_2InB_2 exhibit the largest thermal conductivity values regardless of which relation we used. We found that a $1/T$ dependence of thermal conductivity perfectly matches with the experimental findings, which indicates the dominant role of the Umklapp process up to 1600 K.

ACKNOWLEDGMENTS

This work is supported by the Air Force Office of Scientific Research under award number FA9550-21-1-0208. The main computer resources used in this work are provided by the Computational Research Center at the University of North Dakota and the University of Antwerp (CalcUA), a division of the Flemish Supercomputer Center (VSC), which is funded by the Hercules Foundation. Some of the computations were carried out at NDSU CCAST, which is supported by NSF grants 1229316 and 2019077. S.O.A. wrote some parts of the manuscript and analyzed thermal expansion coefficient and mechanical properties data. B.S. analyzed the data, conducted some of the simulations for thermal conductivity and hardness calculations, and wrote the manuscript. C.S. designed the study and analyzed the data. D.C. designed the study, analyzed the data, conducted the phonon and elastic constant simulations, and wrote the manuscript.

-
- [1] M. Ade and H. Hillebrecht, Ternary borides Cr_2AlB_2 , Cr_3AlB_4 , and Cr_4AlB_6 : The first members of the series $(\text{CrB}_2)_n\text{CrAl}$ with $n = 1, 2, 3$ and a unifying concept for ternary borides as MAB-phases, *Inorg. Chem.* **54**, 6122 (2015).
- [2] S. Kota, M. Sokol, and M. W. Barsoum, A progress report on the MAB phases: Atomically laminated, ternary transition metal borides, *Int. Mater. Rev.* **65**, 226 (2020).
- [3] E. M. Siriwardane, R. P. Joshi, N. Kumar, and D. Çakır, Revealing the formation energy–exfoliation energy–structure correlation of MAB phases using machine learning and DFT, *ACS Appl. Mater. Interfaces* **12**, 29424 (2020).
- [4] H. Becher, K. Krogmann, and E. Peisker, Über das ternäre borid Mn_2AlB_2 , *Z. Anorg. Allg. Chem.* **344**, 140 (1966).
- [5] P. Chai, S. A. Stoian, X. Tan, P. A. Dube, and M. Shatruk, Investigation of magnetic properties and electronic structure of layered-structure borides AlT_2B_2 ($T = \text{Fe}, \text{Mn}, \text{Cr}$) and $\text{AlFe}_{2-x}\text{Mn}_x\text{B}_2$, *J. Solid State Chem.* **224**, 52 (2015).
- [6] Y. Yu and T. Lundström, Crystal growth and structural investigation of the new quaternary compound $\text{Mo}_{1-x}\text{Cr}_x\text{AlB}$ with $x = 0.39$, *J. Alloys Compd.* **226**, 5 (1995).
- [7] J. Wang, T.-N. Ye, Y. Gong, J. Wu, N. Miao, T. Tada, and H. Hosono, Discovery of hexagonal ternary phase Ti_2InB_2 and its evolution to layered boride TIB, *Nat. Commun.* **10**, 2284 (2019).
- [8] L. Verger, S. Kota, H. Roussel, T. Ouisse, and M. Barsoum, Anisotropic thermal expansions of select layered ternary transition metal borides: MoAlB , Cr_2AlB_2 , Mn_2AlB_2 , and Fe_2AlB_2 , *J. Appl. Phys.* **124**, 205108 (2018).
- [9] T. Cabioch, P. Eklund, V. Mauchamp, M. Jaouen, and M. W. Barsoum, Tailoring of the thermal expansion of $\text{Cr}_2(\text{Al}_x, \text{Ge}_{1-x})\text{C}$ phases, *J. Eur. Ceram. Soc.* **33**, 897 (2013).
- [10] X. Wang, K. Chen, E. Wu, Y. Zhang, H. Ding, N. Qiu, Y. Song, S. Du, Z. Chai, and Q. Huang, Synthesis and thermal expansion of chalcogenide MAX phase Hf_2SeC , *J. Eur. Ceram. Soc.* **42**, 2084 (2022).
- [11] S. Kota, M. T. Agne, K. Imasato, T. A. El-Melegy, J. Wang, C. Opagiste, Y. Chen, M. Radovic, G. J. Snyder, and M. W. Barsoum, Effect of texturing on thermal, electric and elastic properties of MoAlB , Fe_2AlB_2 , and Mn_2AlB_2 , *J. Eur. Ceram. Soc.* **42**, 3183 (2022).
- [12] X. Li, X. Xie, J. Gonzalez-Julian, R. Yang, R. Schwaiger, and J. Malzbender, Oxidation and creep behavior of textured Ti_2AlC and Ti_3AlC_2 , *J. Eur. Ceram. Soc.* **42**, 364 (2022).
- [13] B. T. Lejeune, X. Du, R. Barua, J.-C. Zhao, and L. H. Lewis, Anisotropic thermal conductivity of magnetocaloric AlFe_2B_2 , *Materialia* **1**, 150 (2018).
- [14] G. Kresse and J. Hafner, Ab initio molecular dynamics for liquid metals, *Phys. Rev. B* **47**, 558 (1993).
- [15] G. Kresse and J. Furthmüller, Efficient iterative schemes for ab initio total-energy calculations using a plane-wave basis set, *Phys. Rev. B* **54**, 11169 (1996).
- [16] G. Kresse and D. Joubert, From ultrasoft pseudopotentials to the projector augmented-wave method, *Phys. Rev. B* **59**, 1758 (1999).
- [17] G. Kresse and J. Furthmüller, Efficient iterative schemes for ab initio total-energy calculations using a plane-wave basis set, *Phys. Rev. B* **54**, 11169 (1996).
- [18] M. Ernzerhof and G. E. Scuseria, Assessment of the Perdew–Burke–Ernzerhof exchange–correlation functional, *J. Chem. Phys.* **110**, 5029 (1999).
- [19] J. P. Perdew, K. Burke, and M. Ernzerhof, Generalized gradient approximation made simple, *Phys. Rev. Lett.* **77**, 3865 (1996).
- [20] E. M. D. Siriwardane, T. Birol, O. Erten, and D. Çakır, Nanolaminated Fe_2AB_2 and Mn_2AB_2 ($A = \text{Al}, \text{Si}, \text{Ga}, \text{In}$) materials and the assessment of their electronic correlations, *Phys. Rev. Mater.* **6**, 124005 (2022).
- [21] A. Togo and I. Tanaka, First principles phonon calculations in materials science, *Scr. Mater.* **108**, 1 (2015).
- [22] A. Togo, First-principles phonon calculations with phonopy and phono3py, *J. Phys. Soc. Jpn.* **92**, 012001 (2023).
- [23] Y. Aierken, D. Çakır, C. Sevik, and F. M. Peeters, Thermal properties of black and blue phosphorenes from a first-principles quasiharmonic approach, *Phys. Rev. B* **92**, 081408 (2015).
- [24] C. Wolverton and A. Zunger, First-principles theory of short-range order, electronic excitations, and spin polarization in Ni-V and Pd-V alloys, *Phys. Rev. B* **52**, 8813 (1995).

- [25] M. Dahlqvist and J. Rosen, Chemical order or disorder—A theoretical stability expose for expanding the compositional space of quaternary metal borides, *Mater. Adv.* **3**, 2908 (2022).
- [26] J. Lu, S. Kota, M. W. Barsoum, and L. Hultman, Atomic structure and lattice defects in nanolaminated ternary transition metal borides, *Mater. Res. Lett.* **5**, 235 (2017).
- [27] O. Chaix-Pluchery, A. Thore, S. Kota, J. Halim, C. Hu, J. Rosén, T. Ouisse, and M. Barsoum, First-order Raman scattering in three-layered Mo-based ternaries: MoAlB, Mo₂Ga₂C and Mo₂GaC, *J. Raman Spectrosc.* **48**, 631 (2017).
- [28] W. Buck and S. Rudtsch, *Thermal Properties, Springer Handbook of Metrology and Testing*, Vol. 453 (Springer, Berlin, Heidelberg, 2011).
- [29] S. Kota, E. Zapata-Solvas, A. Ly, J. Lu, O. Elkassabany, A. Huon, W. E. Lee, L. Hultman, S. J. May, and M. W. Barsoum, Synthesis and characterization of an alumina forming nanolaminated boride: MoAlB, *Sci. Rep.* **6**, 1 (2016).
- [30] P. Ravindran, L. Fast, P. A. Korzhavyi, B. Johansson, J. Wills, and O. Eriksson, Density functional theory for calculation of elastic properties of orthorhombic crystals: Application to TiSi₂, *J. Appl. Phys.* **84**, 4891 (1998).
- [31] Y. Bai, X. Qi, X. He, D. Sun, F. Kong, Y. Zheng, R. Wang, and A. I. Duff, Phase stability and weak metallic bonding within ternary-layered borides CrAlB, Cr₂AlB₂, Cr₃AlB₄, and Cr₄AlB₆, *J. Am. Ceram. Soc.* **102**, 3715 (2019).
- [32] T. Kocabaş, D. Çkır, and C. Sevik, First-principles discovery of stable two-dimensional materials with high-level piezoelectric response, *J. Phys.: Condens. Matter* **33**, 115705 (2021).
- [33] Z.-j. Wu, E.-j. Zhao, H.-p. Xiang, X.-f. Hao, X.-j. Liu, and J. Meng, Crystal structures and elastic properties of superhard IrN₂ and IrN₃ from first principles, *Phys. Rev. B* **76**, 054115 (2007).
- [34] M. Born, K. Huang, and M. Lax, Dynamical theory of crystal lattices, *Am. J. Phys.* **23**, 474 (1955).
- [35] A. O. Lyakhov and A. R. Oganov, Evolutionary search for superhard materials: Methodology and applications to forms of carbon and TiO₂, *Phys. Rev. B* **84**, 092103 (2011).
- [36] Y. Liu, Z. Jiang, X. Jiang, and J. Zhao, New refractory MAB phases and their 2D derivatives: Insight into the effects of valence electron concentration and chemical composition, *RSC Adv.* **10**, 25836 (2020).
- [37] D. Pettifor, Theoretical predictions of structure and related properties of intermetallics, *Mater. Sci. Technol.* **8**, 345 (1992).
- [38] M. M. Ali, M. Hadi, M. Rahman, F. Haque, A. Haider, and M. Aftabuzzaman, DFT investigations into the physical properties of a MAB phase Cr₄AlB₄, *J. Alloys Compd.* **821**, 153547 (2020).
- [39] R. Hill, The elastic behaviour of a crystalline aggregate, *Proc. Phys. Soc. Sect. A* **65**, 349 (1952).
- [40] S. Kota, M. Agne, E. Zapata-Solvas, O. Dezellus, D. Lopez, B. Gardiola, M. Radovic, and M. W. Barsoum, Elastic properties, thermal stability, and thermodynamic parameters of MoAlB, *Phys. Rev. B* **95**, 144108 (2017).
- [41] D. Connétable and O. Thomas, First-principles study of the structural, electronic, vibrational, and elastic properties of orthorhombic NiSi, *Phys. Rev. B* **79**, 094101 (2009).
- [42] M. Zou, L. Bao, A. Yang, Y. Duan, M. Peng, Y. Cao, and M. Li, Structural, elastic, mechanical, electronic, damage tolerance, fracture toughness, and optical properties of Cr-Al-B MAB phases studied by first-principles calculations, *J. Mater. Res.* **38**, 1396 (2023).
- [43] H. M. Ledbetter, Elastic properties of zinc: A compilation and a review, *J. Phys. Chem. Ref. Data* **6**, 1181 (1977).
- [44] S. I. Ranganathan and M. Ostojca-Starzewski, Universal Elastic Anisotropy Index, *Phys. Rev. Lett.* **101**, 055504 (2008).
- [45] S. Okada, K. Iizumi, K. Kudaka, K. Kudou, M. Miyamoto, Y. Yu, and T. Lundström, Single crystal growth of (Mo_xCr_{1-x})AlB and (Mo_xW_{1-x})AlB by metal Al solutions and properties of the crystals, *J. Solid State Chem.* **133**, 36 (1997).
- [46] K. Kádas, D. Iuşan, J. Hellsvik, J. Cedervall, P. Berastegui, M. Sahlberg, U. Jansson, and O. Eriksson, AlM₂B₂ (M = Cr, Mn, Fe, Co, Ni): A group of nanolaminated materials, *J. Phys.: Condens. Matter* **29**, 155402 (2017).
- [47] A. Ivanovskii, Hardness of hexagonal AlB₂-like diborides of s, p and d metals from semi-empirical estimations, *Int. J. Refract. Met. Hard Mater.* **36**, 179 (2013). Special section: Recent Advances of Functionally Graded Hard Materials.
- [48] X. Jiang, J. Zhao, and X. Jiang, Correlation between hardness and elastic moduli of the covalent crystals, *Comput. Mater. Sci.* **50**, 2287 (2011).
- [49] D. M. Teter, Computational alchemy: The search for new superhard materials, *MRS Bull.* **23**, 22 (1998).
- [50] X. Jiang, J. Zhao, A. Wu, Y. Bai, and X. Jiang, Mechanical and electronic properties of B₁₂-based ternary crystals of orthorhombic phase, *J. Phys.: Condens. Matter* **22**, 315503 (2010).
- [51] N. Miao, B. Sa, J. Zhou, and Z. Sun, Theoretical investigation on the transition-metal borides with Ta₃B₄-type structure: A class of hard and refractory materials, *Comput. Mater. Sci.* **50**, 1559 (2011). Proceedings of the 19th International Workshop on Computational Mechanics of Materials.
- [52] X.-Q. Chen, H. Niu, D. Li, and Y. Li, Modeling hardness of polycrystalline materials and bulk metallic glasses, *Intermetallics* **19**, 1275 (2011).
- [53] E. Mazhnik and A. R. Oganov, A model of hardness and fracture toughness of solids, *J. Appl. Phys.* **126**, 125109 (2019).
- [54] H. Gou, L. Hou, J. Zhang, and F. Gao, Pressure-induced incompressibility of ReC and effect of metallic bonding on its hardness, *Appl. Phys. Lett.* **92**, 241901 (2008).
- [55] S. Singh, L. Lang, V. Dovale-Farelo, U. Herath, P. Tavazde, F.-X. Coudert, and A. H. Romero, Mechelastic: A Python library for analysis of mechanical and elastic properties of bulk and 2D materials, *Comput. Phys. Commun.* **267**, 108068 (2021).
- [56] L. E. Pangilinan, S. Hu, S. G. Hamilton, S. H. Tolbert, and R. B. Kaner, Hardening effects in superhard transition-metal borides, *Acc. Mater. Res.* **3**, 100 (2022).
- [57] S. Lofland, J. Hettlinger, T. Meehan, A. Bryan, P. Finkel, S. Gupta, M. Barsoum, and G. Hug, Electron-phonon coupling in M_{n+1}AX_n-phase carbides, *Phys. Rev. B* **74**, 174501 (2006).
- [58] M. Küpers, P. M. Konze, S. Maintz, S. Steinberg, A. M. Mio, O. Cojocaru-Miréidin, M. Zhu, M. Müller,

- M. Luysberg, J. Mayer, M. Wuttig, and R. Dronskowski, Unexpected Ge-Ge contacts in the two-dimensional Ge₄Se₃Te phase and analysis of their chemical cause with the density of energy (DOE) function, *Angew. Chem., Int. Ed.* **56**, 10204 (2017).
- [59] V. L. Deringer, A. L. Tchougréeff, and R. Dronskowski, Crystal orbital Hamilton population (COHP) analysis as projected from plane-wave basis sets, *J. Phys. Chem. A* **115**, 5461 (2011).
- [60] S. Maintz, V. L. Deringer, A. L. Tchougréeff, and R. Dronskowski, Analytic projection from plane-wave and PAW wavefunctions and application to chemical-bonding analysis in solids, *J. Comput. Chem.* **34**, 2557 (2013).
- [61] S. Maintz, V. L. Deringer, A. L. Tchougréeff, and R. Dronskowski, LOBSTER: A tool to extract chemical bonding from plane-wave based DFT, *J. Comput. Chem.* **37**, 1030 (2016).
- [62] R. Wentorf, R. C. DeVries, and F. Bundy, Sintered superhard materials, *Science* **208**, 873 (1980).
- [63] X. Lu, S. Li, W. Zhang, W. Yu, and Y. Zhou, Thermal shock behavior of a nanolaminated ternary boride: MoAlB, *Ceram. Int.* **45**, 9386 (2019).
- [64] L. Xu, O. Shi, C. Liu, D. Zhu, S. Grasso, and C. Hu, Synthesis, microstructure and properties of MoAlB ceramics, *Ceram. Int.* **44**, 13396 (2018).. A selection of papers presented at CIMTEC 2018.
- [65] S. Kota, M. Agne, E. Zapata-Solvas, O. Dezellus, D. Lopez, B. Gardiola, M. Radovic, and M. W. Barsoum, Elastic properties, thermal stability, and thermodynamic parameters of MoAlB, *Phys. Rev. B* **95**, 144108 (2017).
- [66] S. Kota, M. T. Agne, K. Imasato, T. A. El-Melegy, J. Wang, C. Opagiste, Y. Chen, M. Radovic, G. J. Snyder, and M. W. Barsoum, Effect of texturing on thermal, electric and elastic properties of MoAlB, Fe₂AlB₂, and Mn₂AlB₂, *J. Eur. Ceram. Soc.* **42**, 3183 (2022).
- [67] H. Niu, S. Niu, and A. R. Oganov, Simple and accurate model of fracture toughness of solids, *J. Appl. Phys.* **125**, 065105 (2019).
- [68] H. Niu, S. Niu, and A. R. Oganov, Simple and accurate model of fracture toughness of solids, *J. Appl. Phys.* **125**, 065105 (2019).
- [69] O. L. Anderson, A simplified method for calculating the Debye temperature from elastic constants, *J. Phys. Chem. Solids* **24**, 909 (1963).
- [70] J. Feng, B. Xiao, R. Zhou, W. Pan, and D. R. Clarke, Anisotropic elastic and thermal properties of the double perovskite slab-rock salt layer Ln₂SrAl₂O₇ (Ln = La, Nd, Sm, Eu, Gd or Dy) natural superlattice structure, *Acta Mater.* **60**, 3380 (2012).
- [71] G. Slack, Nonmetallic crystals with high thermal conductivity, *J. Phys. Chem. Solids* **34**, 321 (1973).
- [72] E. S. Toberer, A. Zevkink, and G. J. Snyder, Phonon engineering through crystal chemistry, *J. Mater. Chem.* **21**, 15843 (2011).
- [73] G. Qin, A. Huang, Y. Liu, H. Wang, Z. Qin, X. Jiang, J. Zhao, J. Hu, and M. Hu, High-throughput computational evaluation of lattice thermal conductivity using an optimized Slack model, *Mater. Adv.* **3**, 6826 (2022).